Editors' Suggestion

Magnetic State Control via Field-Angle-Selective Switching in Asymmetric Rings

D. Schönke,[1] R.M. Reeve,[1,2] H. Stoll,[1,3] and M. Kläui[1,2,*]

[1] *Institute of Physics, Johannes Gutenberg-Universität Mainz, 55099 Mainz, Germany*
[2] *Graduate School of Excellence Materials Science in Mainz, Staudinger Weg 9, 55128 Mainz, Germany*
[3] *Max Planck Institute for Intelligent Systems, Heisenbergstraße 3, 70569 Stuttgart, Germany*

(Received 22 June 2020; accepted 14 August 2020; published 10 September 2020)

Ferromagnetic rings have been proposed as an attractive geometry for spintronic storage devices, for instance by storing information in the chirality of the vortex state. Asymmetric rings in particular offer a simple approach to control the vortex-state chirality, and the asymmetry yields additional degrees of freedom for manipulating the states such as by the choice of the field angle with respect to the axes of the system. By using time-resolved scanning electron microscopy with polarization analysis, we directly demonstrate here the influence of the initial magnetization configuration and the field orientation with respect to the ring symmetry axis on the switching mode. The results of experimental imaging are explained by micromagnetic simulations. In particular, for a given field strength we observe switching from the vortex state to the onion state if the symmetry axis of the asymmetric ring is perpendicular to the field orientation. If the symmetry axis deviates slightly from the field orientation, the dynamics change to onion-to-reverse-onion switching with different possible switching pathways. This provides a mechanism for selectively setting different magnetic states by an appropriate choice of the amplitude and orientation of the magnetic field. Furthermore, the angular dependence of the switching is shown to vary with the vortex-state chirality, which could be of use for chirality-dependent logic.

DOI: 10.1103/PhysRevApplied.14.034028

I. INTRODUCTION

In recent years mesoscopic and nanoscale ferromagnetic rings have been the subject of great research interest. Fundamentally they offer particularly stable and simple magnetic states, making them ideal candidate systems for studies of switching dynamics [1]. Furthermore, for possible applications such as storage devices [2], the ring geometry has several advantages compared with other geometries. In the ground state, in the absence of an applied field, the stray field vanishes since the magnetization aligns along the edge and forms a vortex state with either clockwise or counterclockwise chirality, which can be used to store information. In contrast to magnetic disks [3], in rings there is no vortex core with high exchange-energy contributions to the Landau free energy [4], which means this vortex state is particularly stable in rings. An additional metastable remnant state, accessible after application and relaxation of a unidirectional field, is the so-called onion state with opposite circulation of the magnetization in each half of the ring and two 180° domain walls placed at opposite positions [5]. Such a state has a net stray field and magnetization and is of interest for applications where the stray field is used for detecting the magnetic configuration. Mesoscopic and nanoscale magnetic ring geometries have been proposed for various applications, such as memory devices [2,6], spin-based field-effect transistors [7,8], sensors [9,10] and logic applications [11]. Besides stable magnetic states, reliable switching between those states is crucial. For example chirality-dependent logic devices rely on reversing the vortex-state chirality [12], while onion-state-to-reverse-onion-state switching is proposed in lateral giant-magnetoresistance devices [13]. Hence, for maximum flexibility in a device, one would like to be able to switch freely the two vortex-state chiralities, the two onion-state orientations, and between these states controllably and reliably, which would even open up the possibility of concepts such as ring-based multilevel memory cells [14] or multivalued logic [15]. Depending on the size of the ring, there are different switching pathways between the onion state and the reverse onion state by the application of a static uniaxial magnetic field [16]. Rotating fields can also be used to switch the state of the ring, yet from an application point of view uniaxial fields are easier to generate in devices. The onion state can switch to the reverse onion state via rotation of the domain walls or in a two-step process via the flux-closure vortex state [17]. A third option in wider rings is the nucleation of a vortex core in the ring as an intermediate state between the vortex configuration and the onion configuration. A full phase

*klaeui@uni-mainz.de

diagram of the switching mechanisms depending on the ring geometry is given in Ref. [18].

Greater control of the switching pathway in rings can be achieved, for example, by introducing notches [4,19] or by an asymmetric ring (AR) geometry, which offers additional possibilities with single-axis pulse switching compared with symmetric rings. In the AR geometry the inner circle defining the inner perimeter is shifted away from the center of the outer-edge circle. In ARs the onion-state-to-reverse-onion-state switching with uniaxial fields via coherent rotation of the domain walls is suppressed since the narrow part of the ring acts as a trap for one of the domain walls [17]. Switching between the two possible vortex states with opposite chirality in a fully symmetric ring is not easy in a controlled manner with uniaxial fields. However, in ARs this can be accomplished more straightforwardly via nucleating an onion state, followed by so-called automotion of the vortex walls (VWs) along the width gradient toward the narrower part of the ring [20]. Depending on the onion-state direction, either a clockwise vortex or a counterclockwise vortex is the resulting relaxed state after nucleation of one of the onion states [20,21]. Many studies have investigated static or quasistatic hysteresis of rings. However, to understand the full details of the switching mechanisms one needs to resort to time-resolved imaging. For example, the pathways of vortex-to-vortex switching [20], the nucleation of an onion state by homogeneous field pulses [22], and the rotation of onion states [23] have been investigated by time-resolved scanning-transmission x-ray microscopy using rotating fields. A key aspect of AR switching that has so far not been assessed is the influence of the uniaxial-field orientation with respect to the AR symmetry axis on the switching mode as this underlies the selection of the different switching modes. Yet such extra degrees of freedom could provide more functionality and richer behavior for a possible device where the switching is controlled by the choice of the field angle.

In this work we use our recently developed full dynamic scanning electron microscope with polarization analysis (SEMPA) [24] to image the switching dynamics of asymmetric permalloy rings under fast bipolar uniaxial-field pulses. We investigate the dynamic behavior and accessible states for different angles of the field with respect to the symmetry axis of the ARs. The experimental imaging results are explained by micromagnetic simulations. We find in particular that we can control the switching mode and the resulting magnetic configuration of the ARs by choosing an appropriate field angle. Furthermore, we reveal different possible switching pathways in ARs where the symmetry axis is aligned along the magnetic field.

II. SAMPLES AND EXPERIMENT

The samples are fabricated in a two-step electron-beam-lithography and lift-off process using standard poly methyl methacrylate and methyl methacrylate resists. First, the stripline for Oersted-field generation is patterned. It consists of a 3-repetition stack of [Ta(4 nm)CuN(16 nm)] with a Ta(4 nm) capping deposited on a SiO_2 substrate in a Singulus Rotaris sputter chamber. In the next step the ARs are patterned on top of the stripline as shown schematically in Fig. 1(a). $Ni_{80}Fe_{20}$ (30 nm) is deposited by thermal evaporation in a UHV chamber with a base pressure of 10^{-9} mbar. Seven ARs with different symmetry-axis orientations between $\alpha = 0°$ ("AR0") and $\alpha = 90°$ ("AR90") with respect to the orientation of the magnetic field are patterned. The angle between the field and the AR symmetry axis is defined in Fig. 1(a). The outer diameter of the rings is 5.5 μm, the inner diameter is 4.0 μm, and the center of the inner circle is displaced by 400 nm in the direction of the tilt angle α. After conventional static imaging to determine the as-grown configuration and the response of the magnetization after single bipolar-pulse bursts, as shown in Fig. 1(b), the ARs are imaged dynamically during continuous excitation by bipolar Oersted-field pulses in a pump-probe approach, as described in Ref. [24]. Two subsequent opposite-polarity current pulses with a pulse

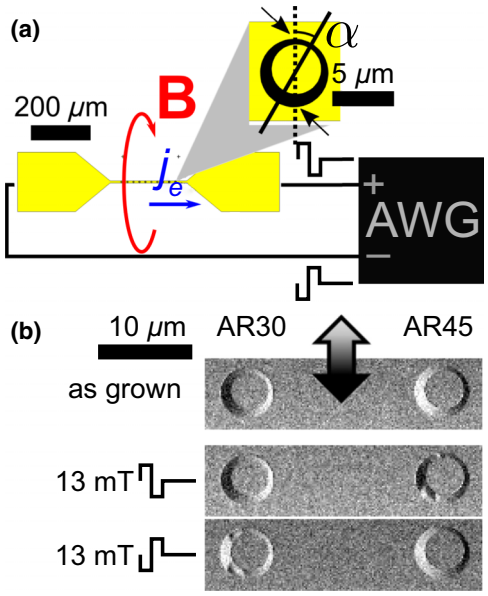

FIG. 1. (a) Schematic setup of the experiment and the sample geometry. An arbitrary-waveform generator (AWG) is the source of the bipolar pulses. The ARs are placed on the stripline with different angles α between their symmetry axis and the stripline axis. The "vertex" position of the VWs in the onion state is indicated by small black arrows. (b) Static y-component magnetic SEMPA images of AR30 with counterclockwise chirality and AR45 with clockwise chirality in the as-grown state, and the remnant configurations after a single excitation cycle consisting of one positive bipolar pulse (up-down) with $B_{max} = 13$ mT and a reverse single excitation of a negative bipolar pulse (down-up). The pulse shape is indicated schematically at the left, and the arrow grayscale bar visualizes the contrast. The resulting state depends on the initial vortex chirality of the ring.

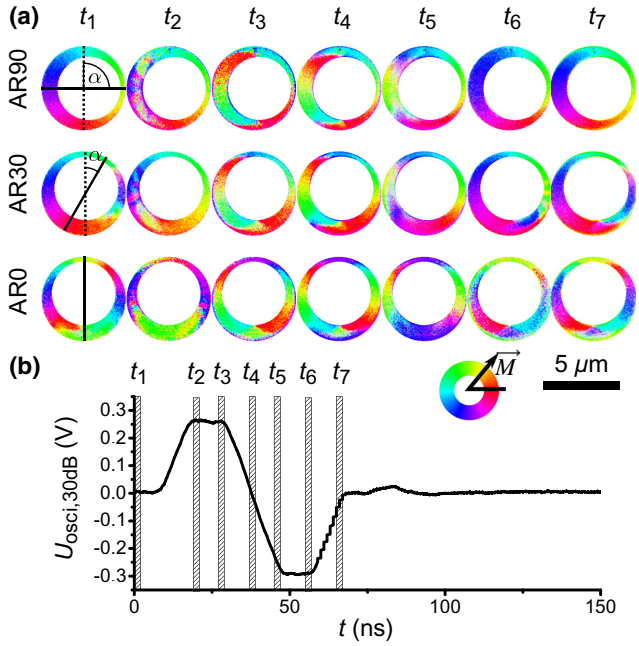

FIG. 2. (a) Selected time frames of the color-coded SEMPA videos for AR90, AR30, and AR0. AR90 exhibits vortex-to-onion-to-vortex switching, while the ARs whose symmetry axis is tilted more toward the field axis exhibit onion-to-reverse-onion-to-onion switching. The color wheel is shown at the right below the images. (b) The excitation pulse with 30-dB attenuation measured after the sample, with the indicated times of the frames shown in (a).

width of 21 ns (FWHM) and a fall and rise time of 8 ns generate an Oersted field of ±15 mT perpendicular to the stripline orientation, with a duty cycle of 39%. By use of an asymmetric driving voltage, as indicated in Fig. 1(a), the sample is maintained at a virtual ground to allow imaging during the continuous excitation without electrostatic variation of the potential of the measured structure. The period of the pulse cycle is 150 ns. The full shape of the current excitation is shown in Fig. 2(b). The SEMPA acquisition is performed with a sampling of 75 frames per excitation period, (i.e., a temporal resolution of 2 ns). The SEMPA system detects simultaneously both the x component and the y component of the magnetization, providing the full in-plane-magnetization-vector information [25]. During the dynamic imaging, the field of view is scanned several hundred times with a pixel dwell time of 2 ms and then drift correction is performed to avoid blurring of the individual scans due to thermal drift of the sample. In the postprocessing, these single scans are cross-correlated and added up. The excitation-correlated displacements of the field of view in the 75 time frames are corrected in the same way. Complementary micromagnetic simulations are performed with the open-source PYTHON-based MICROMAGNUM [26]. The initial magnetization configuration is set either by our defining the chirality of the vortex state and allowing the system to relax or by our taking an onion state generated by applying a bipolar pulse starting from an initial vortex state. The dimensions in the simulations correspond to the dimensions of the experimental samples. The excitation-pulse shape corresponds to the experimental one recorded with a pulse rise time of 8 ns and a width of 21 ns (FWHM). The transient magnetic state is extracted each nanosecond. To simulate the dynamics in the ARs, the typical material parameters of permalloy are used: exchange stiffness $A = 1.3 \times 10^{-11}$ J/m, saturation magnetization $M_S = 800 \times 10^3$ A/m, damping parameter $\alpha = 0.008$, no net magnetocrystalline anisotropy, and a cell size of $5 \times 5 \times 30$ nm^3 [20].

III. RESULTS

First we look at the remnant state after applying a single excitation cycle of one bipolar pulse using conventional static SEMPA imaging. In Fig. 1(b) SEMPA images of the y component of the magnetization for two exemplary ARs with $\alpha = 30°$ and 45° are shown. The upper image in Fig. 1(b) shows the as-grown magnetization state: AR30 is in the counterclockwise vortex state and AR45 in the clockwise vortex state. The image in the center of Fig. 1(b) shows the corresponding magnetic SEMPA image after a single excitation cycle with a field pulse height of 13 mT. The polarity of the bipolar pulse is indicated at the left side images. AR30 is in the counterclockwise vortex state but AR45 has changed to the negative onion state. The lower image in Fig. 1(b) shows the magnetization after a second excitation cycle with the opposite polarity. Now AR30 is in the onion configuration and AR45 is back in the clockwise vortex state. For all investigated rings with ring angles such that they undergo switching between the vortex state and the onion state, a similar correlation of the switching, chirality, and pulse polarity is seen: namely, the counterclockwise state switches to the positive onion state for a negative bipolar pulse (down-up) and the clockwise state switches to the negative onion state for a bipolar pulse of the opposite polarity (up-down). Otherwise the initial vortex state is not changed.

Next we investigate the switching pathway of the ARs by direct time-resolved SEMPA imaging during continuous excitation. The initial state of all ARs is a counterclockwise vortex before the pulse trains are started. Figure 2(a) shows selected frames of the SEMPA videos for AR90, AR30, and AR0 at times t_1–t_7, as indicated on the excitation pulse plotted in Fig. 2(b). The full SEMPA videos can be found in Supplemental Material [27]. First we look at the steady-state after the second pulse (t_7). While for AR90 (and AR45, not shown here) the AR is back in the vortex state with the same chirality as the initial state, for the rings with a lower tilt angle the resulting state is a negative onion state with the net magnetization

pointing in the $-y$ direction. Therefore, during the continuous excitation the magnetization configuration of AR30 and AR0 at the onset of the first pulse at t_1 is also a negative onion state. For all ARs during the first pulse two VWs are nucleated (t_2). If the ring is not symmetric with respect to the field axis, the nucleation occurs in the wider half of the ring, where the initial magnetization direction opposes the applied field due to the counterclockwise vortex configuration. For AR0 and AR30 the initial two walls are annihilated and two new walls are nucleated during the first pulse. In all cases the nucleated walls are moved by the fields, resulting in a positive onion state (t_3). For AR90 and AR30 the switching happens via the formation of a ripplelike concertina pattern in the left half of the AR [22] (t_2). In the case of AR0, this nucleation process is visible at both sides due to the symmetry.

During the first pulse, the VWs in all ARs move to the vertices between the ring and the field axis ["vertex" positions indicated in Fig. 1(a)]. The vortex cores of the VWs are pushed toward the outer perimeter by the field and move more slowly to the vertex (t_3). When the field decreases, the vortex cores move back to the center of the wire (t_4). However for AR90 and AR30 they are still in the left, wider half of the AR. Therefore, during the following inverted pulse, the VWs are pushed back and the VWs annihilate again in the wider half of the AR (t_5–t_6). For AR0 the magnetization dynamics at the vertices is not clear from the experimental image frame at t_5 due to the superposition of different switching pathways, as discussed later. However, for AR30 and AR0, again VWs nucleate during the second pulse (t_6) and a negative onion state forms (t_7), with the negative onion state forming earlier in AR0 (t_6) than in AR30. With the same excitation pattern, AR90 and AR45 show vortex-to-onion-to-vortex switching and the ARs with $\alpha \leq 30^\circ$ show onion-to-reverse-onion-to-onion switching.

In addition to the time-resolved imaging, dynamic micromagnetic simulations are performed and compared with the acquired SEMPA videos to understand the switching processes occurring. In particular, they allow us to compare the dynamic behavior for different initial configurations that are not all accessed in the experiment. The initial frames, as well as the frames directly after each of the pulses, are shown in Fig. 3. Again the full simulation with all time frames is provided in Supplemental Material [27]. Micromagnetic simulations allow us to vary the initial states as well as the intermediate steady-state configurations at different times during the excitation. For the geometry of AR90, two simulations are performed. The first one (simulation 1) starts with an initial counterclockwise vortex state as is the case in the experiment (t_1). During the first pulse a positive onion state is generated as in the experiment (t_4). However, the VWs move into the right half of the ring and annihilate there during the second pulse, while in the wider half a new pair of

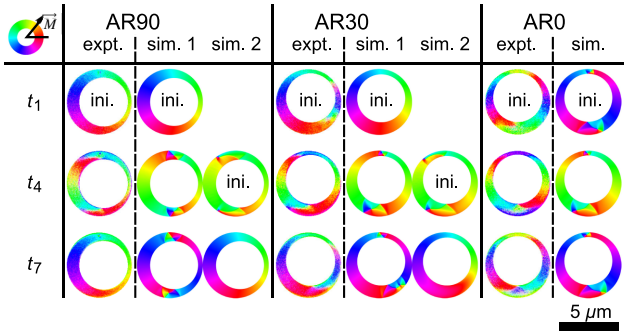

FIG. 3. Comparison of dynamic experimental SEMPA and simulation image frames before and after each pulse for AR90, AR30, and AR0. For AR90 and AR30, two simulations are done: simulation 1 (sim. 1) with the experimental state of t_1 as the initial state (ini.) and simulation 2 (sim. 2) with the state at t_4 as the initial state. The first one diverges from the observed experimental switching pathway because the VWs move further during the first pulse in the simulations and as a result during the second pulse they can move toward the right, narrower side of the AR, while in the experiment the VWs annihilate in the wider half.

VWs is nucleated and the system forms again an onion state with the opposite direction (t_7). A second simulation (simulation 2) starting at t_4 and considering only the dynamics during the second inverted pulse is initialized with an onion state, where the VW positions correspond to the experimentally observed VW positions. In this case the second pulse switches AR90 back to a counterclockwise vortex configuration, as seen in the SEMPA images (t_7).

For AR30 we choose to start the first simulation also with the counterclockwise vortex configuration (t_1), since the two existing VWs visible in the narrower half of the experimental AR at t_1 annihilate directly after the onset of the first pulse and the nucleation of the new VW pair happens in the left, wider half of the ring, forming an onion state (t_4). Again the simulation is qualitatively consistent with the experimental SEMPA images during the first pulse, but the VWs—especially the upper one—move further toward the right in the simulation than in the experiment. Thus, the dynamics during the reversed pulse is again simulated twice: the continuation of simulation 1 shows onion-to-reverse-onion switching via 180° rotation of the domain walls with one of the VWs splitting into a double VW during the motion (t_7) and later merging again (see the full video in Supplemental Material [27]). The second simulation of AR30, which considers just the second pulse and starts with the two VWs at the same positions in the ring as seen in the SEMPA measurement, shows switching back to a counterclockwise vortex state. For AR30 both simulations do not show the onion-to-reverse-onion switching via renucleation of domain walls as is the case for the experimental ring. These different results for different simulations and the experimental comparison

shows the importance of studying the switching experimentally, as the intuitively used simulations yield magnetic states that are not realistic for real samples.

The initial onion configuration of AR0 for the dynamic simulation is achieved by our applying the first pulse to AR0 starting with the counterclockwise vortex state. The VW position can not be determined from the experimental images due to the superposition of two different pathways, as discussed later. In the simulation of the magnetization dynamics of AR0, the upper VW is trapped in the narrow part of the ring. During the pulse, the lower VW is moved toward the upper VW and annihilates there, while in the other half of the AR a new pair of VWs nucleate and another onion state forms. The general onion state-to-reverse-onion-state switching is observed in the experiment as well as in the simulation if the symmetry axis is parallel to the field axis.

Additionally, for all ring geometries and cases with an onion state at t_7, the simulations show gradient-driven automotion of the VWs toward the narrowest part of the ring in the time when no field is applied (see Supplemental Material [27]). We perform selected additional simulations with a slightly increased damping parameter ($\alpha = 0.014$, not shown). These simulations exhibit less automotion, showing that control of the damping of the system would be an additional way to tailor the exact behavior of the device.

As shown in Ref. [28], additional information on the switching-pathway reliability is revealed in the single-scan images during the SEMPA acquisition. In particular, changes between different switching pathways are visible if the frequency of these changes is lower than the scan frequency. Figure 4(a) shows exemplary SEMPA single-scan magnetic-x-component images. The ARs with higher tilt angles show a clear vortex state. For AR30, AR15, and AR0 sudden contrast jumps interrupt the overall negative onion state at the AR vertices. If the AR symmetry axis determined by the angle α gets close to the field axis, VWs can be nucleated at both sides of the AR. Therefore, two switching pathways are possible with thermal excitations leading to one or the other. The remnant VW position depends on the nucleation side. The sudden contrast jumps at the vertices of the ARs are a signature of a change between the two possible switching pathways. The respective relative pathway probability is estimated by our fitting two Gaussian functions to each histogram of the pixel x-asymmetry values in the red region of interest as shown in Fig. 4(b).

IV. DISCUSSION

The static SEMPA images of ARs after application of a single bipolar pulse indicate a chirality-dependent switching probability for the magnetic field strength used in this study. The field necessary to generate a positive or negative onion configuration from the vortex state is asymmetric and depends on the chirality of the initial vortex state. Therefore, in general, for onion-to-reverse-onion switching higher fields are required in ARs if the symmetry axis is not parallel to the field orientation. The full SEMPA videos reveal the detailed switching behavior and also the reason for this asymmetry, which originates from the asymmetry of the ring itself. The ARs with a tilt angle greater than 30° switch reliably from a counterclockwise vortex to a positive onion state and back. The nucleation of a VW pair in the narrower half of the AR is energetically not possible because of the small width of the ring, and therefore domain walls can be nucleated only from the vortex state during a field pulse when it is aligned opposite to the magnetization in the wider half of the ring. This means the switching does not show 180° symmetry with respect to the field angle, or in other words, for a given field angle, the switching depends on the vortex-state chirality. In contrast to the simulation (simulation 1), in the experiment the field does not move the VWs beyond the vertex. Here the VWs are pushed back to the widest part of the ring and annihilate there. The stronger motion of the VWs in the simulation is attributed to the fact that in the simulations material imperfections are not included and therefore pinning is reduced, showing that the intuitively used simulations of perfect materials do not reproduce the experimental results. Besides pinning, an enhanced damping parameter also counteracts the automotive force. By rotation of the AR with respect to the field direction, the average width of the right side of the ARs increases and thereby also the probability of VW nucleation. In AR30 the nucleation does not occur symmetrically around 90° but is shifted toward the lower and thus wider part of the ring. For AR30 the simulation (simulation 2) does not show onion-to-reverse-onion-to-onion switching, since it calculates the magnetization dynamics without including thermal effects. In the experiment, the nucleation of the VWs during the formation of the reverse onion state is supported by thermal excitations. For even lower tilt angles, the upper VW is trapped in the narrow part of the AR and the lower VW moves around 180° until it annihilates with the upper VW. Including thermal fluctuations in the micromagnetic simulations would be a possible route toward a deeper understanding of these temperature-induced effects. In the dynamic SEMPA video of AR0 (and AR15, not shown), which integrates the signal over all pulse cycles, simultaneous nucleation at both sides is visible. However, the single-scan images in Fig. 4(a) indicate and can differentiate between two different switching pathways for these ARs. Both possible pathways result in the respective onion state, but the nucleation occurs either at the left side or at the right side of the ring. Since the VWs do not reach the vertex in the experiment but stop before it, these white and black stripes in the single-scan images appear [Fig. 4(a)]. The video is integrated over all excitation cycles during

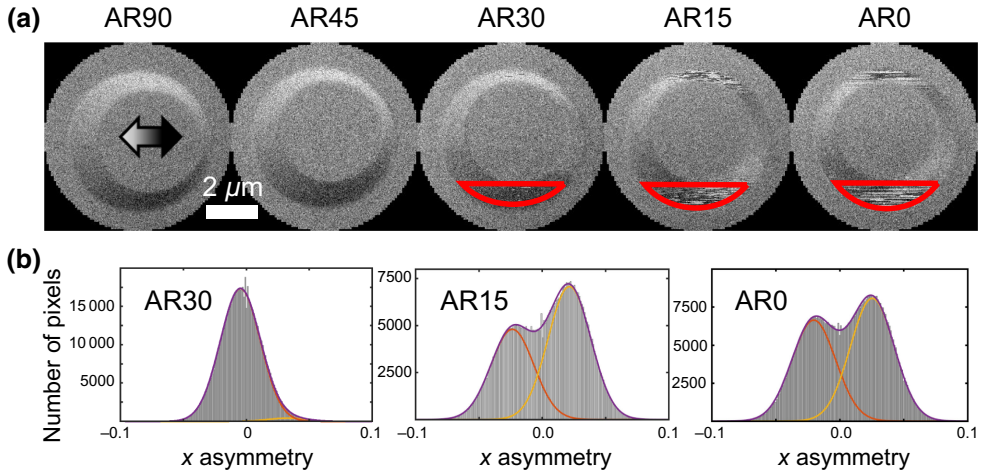

FIG. 4. (a) Exemplary SEMPA single-scan x-component images. AR90 and AR45 show a clear counterclockwise vortex configuration, while AR15 and AR0 show an onion state. In the single scans of the ARs with $\alpha \leq 30^\circ$, abrupt contrast changes are visible, indicating changes of the switching pathway. The red-marked region of interest in AR30, AR15, and AR0 is the area used to determine the relative occurrence of the different pathways. (b) Histogram showing the value of each pixel asymmetry value. A superposition of two Gaussian functions is fitted to the histogram. The ratio of the areas below each Gaussian function is a measure of the relative occurrence of both pathways.

all acquired scans and shows different switching pathways with similar probability superimposed. For AR30 the pathway with the nucleation in the right half of the ring during the second pulse is still strongly suppressed with a probability of just 2%. In AR15 the probability of this pathway accounts for 60% and in AR90 for 55%. This also explains the apparent synchronous VW nucleation at both sides in AR0 in the video as shown in Fig. 2. The comparable probability of both switching pathways determined by our fitting the double Gaussian to the x-asymmetry histogram confirms this hypothesis. The change from one pathway to the other can occur via thermally excited increased motion of the VWs so that they overcome the pinning and move beyond the vertex on rare occasions in the experiment, as seen in the simulations without pinning, after which they annihilate in the opposite side of the AR from where they are nucleated, changing the state for the next cycle. In general, such stochastic effects should be suppressed in devices that are expected to work with very high reliability. However, the two states adopted by the AR between the excitation pulses are the same for both pathways, which is key for successful applications that use the magnetic state to encode the data. While generating local magnetic fields along an arbitrary axis, which is required for field-angle-dependent switching, is technologically challenging in small structures, the advantage of ring-based devices is the simple geometry and the high scalability.

V. CONCLUSION

We study the dependence of switching between magnetic states in permalloy ARs for magnetic fields applied along different selected directions with respect to the symmetry axes of the ARs. We find we can selectively tune the switching from vortex-to-onion-to-vortex switching to another switching mode starting with an onion state, switching to a reverse onion state and then back to the original onion state with the initial chirality just by judiciously choosing the field angle. The critical angle defining the switching behavior for the given field is 30°. With our measurements we identify different possible switching pathways with approximately equal probability if the symmetry axis of the AR deviates by less than 30° from the field axis. However, this does not change the general resulting magnetic state. If the field is aligned in a direction more perpendicular to the AR symmetry axis, the chirality of the initial vortex state helps or impedes the formation of an onion state, depending on its polarity, resulting in full deterministic switching via a single pathway. The choice of the field angle in such ARs thereby provides a convenient way to reliably select multiple different states. Magnetic state control via selection of the field angle could be of use for applications such as stray-field-based rotation sensors, chirality-dependent logic, or multistate computing devices.

ACKNOWLEDGMENTS

We acknowledge financial support of SFB/TRR 173 Spin+X: Spin in Its Collective Environment funded by the Deutsche Forschungsgemeinschaft - TRR 173 - 268565370 and project Grant No. KL1811/18 (318612841), as well as the Graduate School of Excellence Materials Science in Mainz (Grant No. GSC266) and the European Research Council (Grant No. ERC-2019-SyG #856538 3D MAGiC).

[1] M. Kläui, Head-to-head domain walls in magnetic nanostructures, J. Phys.: Condens. Matter **20**, 313001 (2008).

[2] J.-G. Zhu, Y. Zheng, and G. A. Prinz, Ultrahigh density vertical magnetoresistive random access memory, J. Appl. Phys. **87**, 6668 (2000).

[3] T. Shinjo, T. Okuno, R. Hassdorf, K. Shigeto, and T. Ono, Magnetic vortex core observation in circular dots of permalloy, Science **289**, 930 (2000).

[4] M. Kläui, J. Rothman, L. Lopez-Diaz, C. A. F. Vaz, J. A. C. Bland, and Z. Cui, Vortex circulation control in mesoscopic ring magnets, Appl. Phys. Lett. **78**, 3268 (2001).

[5] J. Rothman, M. Kläui, L. Lopez-Diaz, C. A. F. Vaz, A. Bleloch, J. A. C. Bland, Z. Cui, and R. Speaks, Observation of a Bi-Domain State and Nucleation Free Switching in Mesoscopic Ring Magnets, Phys. Rev. Lett. **86**, 1098 (2001).

[6] Xiaochun Zhu and Jian-Gang Zhu, A vertical MRAM free of write disturbance, IEEE Trans. Magn. **39**, 2854 (2003).

[7] P. Gallo, A. Arnoult, T. Camps, E. Havard, C. Fontaine, L. Lombez, T. Amand, X. Marie, and A. Bournel, Self-aligned and stray-field-free electrodes for spintronics: An application to a spin field effect transistor, J. Appl. Phys. **101**, 024322 (2007).

[8] J. H. Lee, S. N. Holmes, B. Hong, P. E. Roy, M. D. Mascaro, T. J. Hayward, D. Anderson, K. Cooper, G. A. C. Jones, M. E. Vickers, C. A. Ross, and C. H. W. Barnes, Magnetic remanent states and quasistatic switching behavior of Fe split-rings for spin field-effect-transistor applications, Appl. Phys. Lett. **95**, 172505 (2009).

[9] M. M. Miller, G. A. Prinz, S.-F. Cheng, and S. Bounnak, Detection of a micron-sized magnetic sphere using a ring-shaped anisotropic magnetoresistance-based sensor: A model for a magnetoresistance-based biosensor, Appl. Phys. Lett. **81**, 2211 (2002).

[10] B. Borie, J. Wahrhusen, H. Grimm, and M. Kläui, Geometrically enhanced closed-loop multi-turn sensor devices that enable reliable magnetic domain wall motion, Appl. Phys. Lett. **111**, 242402 (2017).

[11] A. Imre, L. Zhou, A. Orlov, G. Csaba, G. H. Bernstein, W. Porod, and V. Metlushko, in *4th IEEE Conference on Nanotechnology, 2004* (2004), p. 137.

[12] S. R. Bowden, K. K. L. Ahmed, and U. J. Gibson, Longitudinal magneto-optic kerr effect detection of latching vortex magnetization chirality in individual mesoscale rings, Appl. Phys. Lett. **91**, 232505 (2007).

[13] S. Jain and A. O. Adeyeye, Probing the magnetic states in mesoscopic rings by synchronous transport measurements in ring-wire hybrid configuration, Appl. Phys. Lett. **92**, 202506 (2008).

[14] S. Matsunaga, K. Hiyama, A. Matsumoto, S. Ikeda, H. Hasegawa, K. Miura, J. Hayakawa, T. Endoh, H. Ohno, and T. Hanyu, Standby-power-free compact ternary content-addressable memory cell chip using magnetic tunnel junction devices, Appl. Phys. Express **2**, 023004 (2009).

[15] G. Epstein, G. Frieder, and D. C. Rine, The development of multiple-valued logic as related to computer science, Computer **7**, 20 (1974).

[16] M. Kläui, C. A. F. Vaz, J. A. C. Bland, T. L. Monchesky, J. Unguris, E. Bauer, S. Cherifi, S. Heun, A. Locatelli, L. J. Heyderman, and Z. Cui, Direct observation of spin configurations and classification of switching processes in mesoscopic ferromagnetic rings, Phys. Rev. B **68**, 134426 (2003).

[17] M. Kläui, C. A. F. Vaz, L. Lopez-Diaz, and J. A. C. Bland, Vortex formation in narrow ferromagnetic rings, J. Phys.: Condens. Matter **15**, R985 (2003).

[18] M. Kläui, C. Vaz, L. Heyderman, U. Rüdiger, and J. Bland, Spin switching phase diagram of mesoscopic ring magnets, J. Magn. Magn. Mater. **290-291**, 61 (2005).

[19] L. Lopez-Diaz, M. Kláui, J. Rothman, and J. Bland, Fast and controllable switching in narrow ring nanomagnets, J. Magn. Magn. Mater. **242–245**, 553 (2002).

[20] M.-A. Mawass, K. Richter, A. Bisig, R. M. Reeve, B. Krüger, M. Weigand, H. Stoll, A. Krone, F. Kronast, G. Schütz, and M. Kläui, Switching by Domain-Wall Automotion in Asymmetric Ferromagnetic Rings, Phys. Rev. Appl. **7**, 044009 (2017).

[21] F. Q. Zhu, G. W. Chern, O. Tchernyshyov, X. C. Zhu, J. G. Zhu, and C. L. Chien, Magnetic Bistability and Controllable Reversal of Asymmetric Ferromagnetic Nanorings, Phys. Rev. Lett. **96**, 027205 (2006).

[22] K. Richter, A. Krone, M.-A. Mawass, B. Krüger, M. Weigand, H. Stoll, G. Schütz, and M. Kläui, Localized domain wall nucleation dynamics in asymmetric ferromagnetic rings revealed by direct time-resolved magnetic imaging, Phys. Rev. B **94**, 024435 (2016).

[23] K. Richter, A. Krone, M.-A. Mawass, B. Krüger, M. Weigand, H. Stoll, G. Schütz, and M. Kläui, Local Domain-Wall Velocity Engineering via Tailored Potential Landscapes in Ferromagnetic Rings, Phys. Rev. Appl. **5**, 024007 (2016).

[24] D. Schönke, A. Oelsner, P. Krautscheid, R. M. Reeve, and M. Kläui, Development of a scanning electron microscopy with polarization analysis system for magnetic imaging with ns time resolution and phase-sensitive detection, Rev. Sci. Instrum. **89**, 083703 (2018).

[25] H. P. Oepen, G. Steierl, and J. Kirschner, Scanning electron microscope with polarization analysis: Micromagnetic structures in ultrathin films, J. Vac. Sci. Technol. B **20**, 2535 (2002).

[26] https://github.com/MicroMagnum/MicroMagnum/

[27] See Supplemental Material at http://link.aps.org/supplemental/10.1103/PhysRevApplied.14.034028 for the full videos of the SEMPA measurements and the simulations.

[28] D. Schönke, R. M. Reeve, and M. Kläui, Quantification of competing magnetic states and switching pathways in curved nanowires by direct dynamic imaging, arXiv:2006.11271.